

## RESEARCH ARTICLE

10.1029/2017JB015105

## Key Points:

- Mechanical tests with ultrasonic data of heat-treated, dry and saturated limestones
- Results revealed water and temperature dependence at the brittle-ductile transition
- Integrated in a 2D model, results highlight broad impacts for some volcanic basements

## Supporting Information:

- Supporting Information S1

## Correspondence to:

A. Castagna,  
ac605@ac.le.uk

## Citation:

Castagna, A., Ougier-Simonin, A., Benson, P. M., Browning, J., Walker, R. J., Fazio, M., & Vinciguerra, S. (2018). Thermal damage and pore pressure effects of the brittle-ductile transition in comiso limestone. *Journal of Geophysical Research: Solid Earth*, 123, 7644–7660. <https://doi.org/10.1029/2017JB015105>








Received 12 OCT 2017

Accepted 12 JUN 2018

Accepted article online 26 JUN 2018

Published online 27 SEP 2018

## Thermal Damage and Pore Pressure Effects of the Brittle-Ductile Transition in Comiso Limestone

A. Castagna<sup>1</sup> , A. Ougier-Simonin<sup>2</sup> , P. M. Benson<sup>3</sup> , J. Browning<sup>4</sup> , R. J. Walker<sup>1</sup> , M. Fazio<sup>3,5</sup> , and S. Vinciguerra<sup>6</sup> 

<sup>1</sup>Department of Geology, University of Leicester, UK, <sup>2</sup>Rock Mechanics and Physics Laboratory, British Geological Survey, Nottingham, UK, <sup>3</sup>Rock Mechanics Laboratory, University of Portsmouth, UK, <sup>4</sup>Rock and Ice Physics Laboratory, Department of Earth Sciences, UCL, UK, <sup>5</sup>Department of Applied Geology, University of Göttingen, Germany, <sup>6</sup>Department of Earth Sciences, University of Turin, Italy

**Abstract** Volcanic edifices are commonly unstable, with magmatic and non-magmatic fluid circulation, and elevated temperature gradients having influence on the mechanical strength of edifice and basement rocks. We present new mechanical characterization of the Comiso limestone of the Mount Etna Volcano (Italy) basement to constrain the effects of regional ambient conditions associated with the volcanic system: the effects of pore fluid on rock strength and the effects of distal magmatic heating (~20 °C to 600 °C) at a range of simulated depths (0.2 to 2.0 km). The presence of water promotes ductile behaviour at shallow depths and causes a significant reduction in brittle rock strength compared to dry conditions. Thermal stressing, in which specimens were heated and cooled before mechanical testing at room temperature, has a variable effect for dry and saturated cases. In dry conditions, thermal stressing up to 450 °C homogenizes the strength of the specimen such that the majority of the specimens exhibit the same peak stress; at 600 °C, the brittle failure is promoted at lower differential stress. The presence of water in thermally-stressed specimens promotes ductile behaviour and reduces peak strength. Acoustic emission monitoring suggests that accumulated damage is associated with the heating-cooling sequence, particularly in the 300–450–600°C. Based on conduction modeling, we estimate this temperature range could affect basement rocks up to 300 m away from minor sheet intrusions and much further with larger bodies. Considering the dyke spacing beneath Etna, these conditions may apply to a significant percentage of the basement, promoting ductile behaviour at relatively shallow depths.

**Plain Language Summary** Volcanoes can collapse as a result of underground magma, gas and/or water flows, and temperature effects on its basement rock's strength. We did laboratory experiments to further test the strength of surface samples of a limestone present beneath Mount Etna Volcano (Italy). We kept some samples 'as-collected' and heated and cooled the others at different temperatures (up to 600°C) prior to their deformation as if some magma bodies had flown in the vicinity of these rocks. We then water saturated a sample of each temperature condition applied and compared their strengths at different simulated depths ranging about 0.2 to 2.0 km (i.e. confinement ranging between 7 and 50 MPa) to the ones of the corresponding samples kept dry. Our results show that water presence lowers the limestone strength compared to dry conditions but also the conditions of pressure at which the failure behaviour transitions between brittle and ductile regimes. For temperature up to 450 °C, the strength of this limestone seems to be independent of the treatment's temperature with the maximum strength values being higher in dry conditions than in water saturated conditions. The rock fails only in the brittle regime when thermally treated prior deformation at all temperatures, saturation and confinement applied. Considering the dyke spacing beneath Mount Etna, these combinations of water, temperature and pressure conditions may apply to a significant percentage of the basement, promoting weaker and ductile behaviour at relatively shallow depths.

## 1. Introduction

Volcanic environments are subjected to many processes that can cause weakening of the edifice and of the underlying basement (e.g. De Vries & Borgia, 1996; McGuire, 1996). In particular, magmatic intrusion via dykes and sills or emplacement of larger magma bodies results in damage growth during emplacement (Voight & Elsworth, 1997), changes to the stress state during and following magmatism (Aloisi et al., 2011; Bonaccorso et al., 2010), and high temperature gradients (Bonaccorso et al. (2010)). Transient temperature variation may

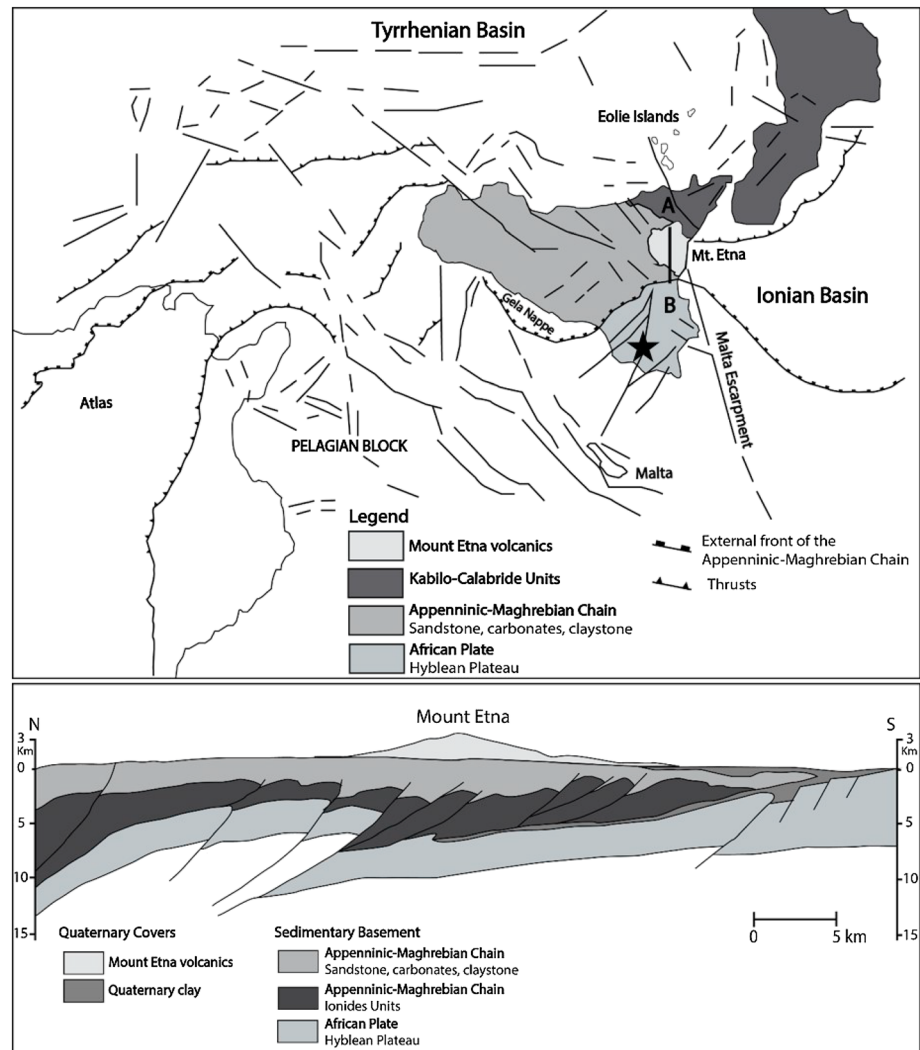


**Figure 1.** Top panel: Illustration of the main structural features and lithological units in and around Sicily (Italy): Dark gray for the Kabilo-Calabride chain, medium gray for the Appenninic-Maghrebian chain, light gray for the Hyblean plateau units, and very light gray for the volcanic units of Mount Etna. The black star locates the CL quarry. Lower panel shows a cross-section along line A-B in the top panel across Mount Etna, highlighting the key stratigraphic and structural relationships in the sedimentary basement of Mount Etna. All modified and simplified after Branca et al., 2011.

lead to the generation of permanent changes to the hosting material, owing to heat-induced mineralogical transitions, hydrothermal alteration, and intrusion-induced fractures. Extreme cases of thermal alteration and weakening can enhance catastrophic flank collapses (e.g. Day, 1996; Dieterich, 1988; Elsworth & Day, 1999; Reid et al., 2001; Voight & Elsworth, 1997). Most studies of such effects focus on the volcanic edifice rocks (e.g. Reid et al., 2001), or on rocks composing the basement (e.g. Bakker et al., 2015; Delaney & Pollard, 1982; Elsworth & Voight, 1992; Heap et al., 2013). Basement rocks typically host some type of pore fluid (water, brine, hydrothermal fluids: e.g. Day, 1996, Mattia et al., 2015, Dautriat et al., 2011), and owing to the distribution of intrusions in subvolcanic systems, much of the sub-edifice basement is likely to be subject to lower – but still elevated – temperatures (i.e. <600 °C).

The presence of a sedimentary substratum under Mount Etna is a known control on the edifice stability for many years (e.g. Mattia et al., 2015; Van Wyk De Vries & Borgia, 1996). The Etnean basement is dominated by a mélange of deformed sandstones, limestones, clays (Appenninic-Maghrebian Chain, Figure 1) and thick carbonate sequences (Hyblean Plateau, African Units; Figure 1) (Branca et al., 2011; Lentini et al., 2006), which have been the subject of previous mechanical characterization (e.g. Bakker et al., 2015; Heap et al., 2013;

Mollo et al., 2011; Wiesmaier et al., 2015). In this study, we select samples from the carbonate units of the Hyblean Plateau and report new results from an experimental investigation that builds on these previous studies. Specifically, we consider the thermal history of subsurface carbonate sequences with new data on fracture damage due to an imposed deformation. Furthermore, we use these data to simulate the thermal damage induced by a dyke intrusion into the country rocks. The chosen range of temperature (150–600 °C) mimics a rock near enough to be subjected to significant temperature transients (not directly in contact with the dyke), which is the case of a large proportion of material in natural conditions. The key questions we seek to address here are: (1) how is induced thermal damage captured by elastic wave velocity and Acoustic Emission (AE), and (2) what is the influence of this thermal history on the mechanical properties with respect to fluid saturation? To achieve this, we infer the input of thermal crack damage from contemporaneous AE measurements during a pre-test thermal treatment (cycle of heating then cooling) up to a maximum of 600 °C, on the Comiso limestone (Hyblean Plateau). Comiso Limestone (CL) was chosen because i) it was already previously investigated (Bakker et al., 2015) and ii) it is a very good analogue for the complexity of the sedimentary substratum. We then compare the mechanical properties of dry and saturated, ‘as collected’ and heat-treated specimens as a function of applied stress and strain via conventional triaxial experiments. This combined suite of data allows us to expand the investigation and discussion of the strength evolution, on the role of water and thermal damage and to better constrain the deformation mechanisms related to the Brittle-Ductile Transition (BDT).

## 2. Background

Mount Etna volcano sits atop a structurally complex sedimentary basement. Etnean basement is dominated by formations consisting of sandstone, limestone, and clay that are part of the wider Appenninic-Maghrebain Chain (AMC). The AMC is part of the accretionary wedge of a regional fold-and-thrust belt that lies above the carbonate Hyblean Plateau (HP) sequences, which is part of the African plate (Figure 1). The sedimentary covers of the HP present an average thickness of 6 km, and consist of mainly carbonate sequences (Mesozoic – Cenozoic) with volcanic intercalations: we selected carbonate samples from the Ragusa Formation (Branca et al., 2011; Lentini et al., 2006; black star, Figure 1) for our tests.

Geophysical models of the Mount Etna plumbing system suggest that an intermediate magma storage body exists at approximately 4–8 km b.s.l. (e.g. Aloisi et al., 2011; Bonaccorso et al., 2005), which would place it partly within the sedimentary basement, rather than the dominantly basaltic edifice. This magma body affects the surrounding sedimentary rocks due to its elevated temperature, ranging from >1000 °C at the contact decreasing to 300 °C at a distance of about 1.5 km (Mollo et al., 2011).

From a mechanical perspective, the effect of elevated temperature on carbonate rocks is known to be a function of several parameters including grain size, porosity, and strain rate (e.g. Rutter, 1972, 1974; Siegesmund et al., 2000). Recently, new data extended this knowledge to investigate the effect of high temperatures on triggering physical and chemical reactions via decarbonisation (e.g. Bakker et al., 2015; Heap et al., 2013; Mollo et al., 2011). In one of these studies the physical and mechanical properties of two limestones (Climiti and Thala units (Heap et al. (2013)) were investigated in uniaxial and at *in situ* elevated temperature conditions. Both materials underwent decarbonisation reactions, with a total mass loss of 45% occurring between 560–900 °C, which accompanied a drastic change of the limestone physical properties. Increasing temperature and pressure resulted in a change in peak stresses in the brittle field, up to 500 °C, above which ductility was promoted (e.g. Bakker et al., 2015), as the specimens started to ‘flow’ in an aseismic manner, with a strong dependence of flow stress on temperature (i.e. decreasing in dry elastic moduli, seismic velocities, and acoustic emission rate). It was suggested that such processes may be responsible for the large-scale deformation present at Mount Etna. This hypothesis is further reinforced by observations of clay dehydroxylation (Mollo et al., 2011), along with a decreased strength which is likely to further promote flank instability and explain low seismicity zones, as well as the high local CO<sub>2</sub> overpressures. However, the limitation of these experiments is that they were conducted at ambient pressure conditions, rather than pressures which simulate burial depth. Nicolas et al. (2016) explored the brittle and semi-brittle behaviour of a 14.7% porosity, ~100% calcite Tavel limestone and compared the results with CL in dry and saturated conditions, also using low *in-situ* temperature in an additional

series of dry tests. Tavel limestone showed a brittle behaviour up to 55 MPa followed by a semi-brittle behaviour - defined by Evans et al. (1990) as a macroscopically distributed deformation involving micro-cracking and crystal plasticity - over 55 MPa. Water had a relatively small impact on the strength of Tavel limestone (Nicolas et al., 2016). In addition, recent triaxial experiments performed on CL by Bakker et al. (2015) used representative shallow subsurface volcanic pressure conditions (specifically 50 and 100 MPa representative of 2 and 4 km depth).

Collectively, these studies support the hypothesis that both elevated temperature and pressure have significant effect on the mechanical strength of carbonate rocks. Confining pressure was found to limit the decarbonation reactions as a result of the decreased porosity due to increasing pressures, as well as the increased CO<sub>2</sub> fugacity, which has a major role in controlling the decarbonation process (Mollo et al., 2011). They identify that the brittle-ductile mechanical transition occurs at temperatures of approximately 350 °C, with 50 MPa confining pressure and constant strain rate at 10<sup>-5</sup> s<sup>-1</sup>. In addition to these investigations of induced damage at high temperatures, micro-crack damage is also inferred to occur during heating and cooling (e.g. Browning et al., 2016). This latter effect is important as the injection of dykes and sills clearly expose the country rock to significant temperature gradients. Indeed, the increasing and decreasing amount of heat radiated by an intrusion into a body of country rock very likely play an important role on the rock's temperature-dependent properties and processes, such as decarbonation in limestone, potentially further reflected in the overall deformation observed at the surface.

### 3. Material Characterization and Methodology

#### 3.1. Comiso Limestone and Specimen Preparation

Limestone samples were collected from the Ragusa Formation of the Western Hyblean Plateau, which occurs in monotonic layers that dip gently (335–16°) to the NNW. The Ragusa Formation is accessed in section via outcrops in a quarry near to Comiso village in SE Sicily (Figure 1a, black star). The Ragusa Formation has layers of maximum thickness of 60 cm, and is interlayered with unconsolidated clay-bearing strata. Carbonates from the Ragusa Formation are mainly composed of calcarenites (>50% carbonate grains with a grain size ranging between 0.06 mm to 2 mm) and marls (carbonate-rich soft mudstone with grain size <0.06 mm) of Lower Oligocene age (Lentini & Carbone, 2014). Carbonate within the formation are generally either a combination of calcite (CaCO<sub>3</sub>) and dolomite (CaMg (CO<sub>3</sub>)<sub>2</sub>), or occasionally a pure calcite. A detailed description was provided by Bakker et al. (2015), who reported an initial, average porosity of 8.7%, and density of 2.47 g/cm<sup>3</sup>. The rocks used in this study have an average porosity of 10.1% (measured with a helium pycnometer) and density of 2.47 g/cm<sup>3</sup>. At the intralayer scale, the fabric is isotropic and CL is treated as an essentially homogeneous material. The CL used in this study is composed of calcite (97.7%) and a small amount of quartz (2.3% wt), as determined from X-Ray Diffraction and X-Ray Fluorescence analysis (see Figure S1a in supporting material). All of the specimens used in this study were cored from the same sample using identical coring techniques to minimize specimen variation. In total, 14 cylindrical specimens (40 mm diameter (±0.03 mm) and with a length of 100 mm (± 0.5 mm); Table 1) were cored from the CL sample using a diamond coring drill, and a lathe fitted with a cross-cutting wheel to ensure parallelism to 0.01 mm or better.

#### 3.2. Thermal Treatment

To investigate the effects of thermal stressing on CL properties, a suite of specimens were heated and allowed to cool prior to triaxial deformation tests. A selection of specimens were heat-treated using a high temperature, Carbolite CTF12/75/700 tube furnace (Browning et al., 2016) between 150 °C and 600 °C to induce varying amounts of micro-fracture damage (Figure 2a). The specimens were held within a ~1 m length purpose-built steel jig comprised of rods and springs providing the specimen with a constant end load within the central section of the tube furnace. Temperature was controlled and monitored by a series of thermocouples mounted immediately adjacent to the specimen surface. In all tests, a controlled heating rate of 1 °C/minute was applied, keeping the specimen at the desired maximum temperature for 30 minutes to allow complete temperature equilibration followed by natural cooling (generally less than <1 °C/minute).

**Table 1**

Summary of the Experimental Conditions Used for the Tests on CL and Basic Mechanical Parameters, Including Values of Stress and Strain at Peak Differential Stress, and Values of Differential Stress and Strain at Specimen Failure. The Young's Moduli were Calculated from Best Fit to the Linear Elastic Section Between 0.1–0.2% Axial Strain. Presence of Localized Failure and Non Localized Deformation are Reported in the Last Column

Experiment name	Pconf (MPa)	Pf (MPa)	Depth (m) average density of 2470 kg/m <sup>3</sup>	Thermal treatment (°C)	Peak differential stress (MPa)	Strain at peak differential stress (%)	Young Modulus (GPa)	Stress at failure (MPa)	Strain at failure (MPa)	Presence of failure
1 Dry	7		290	No	116.23	0.52	28.69	108.88	0.58	Localized
1 Sat	12	5	495	No	105.09	0.76	20.02	105.09	0.76	Localized
2 Dry	15		620	No	160.59	0.73	32.27	160.59	0.73	Localized
2 Sat	25	10	1035	No	133.49	1.01	32.43	120.97	1.57	Localized
3 Dry	15		620	150	161.73	0.68	35.65	161.73	0.68	Localized
3 Sat	25	10	1035	150	135.65	0.97	28.96	127.66	1.32	Localized
4 Dry	15		620	300	162.89	0.57	44.66	160.74	0.63	Localized
4 Sat	25	10	1035	300	132.48	0.94	27.24	122.07	1.37	Localized
5 Dry	15		620	450	164.37	0.94	28.08	159.44	1.1	Localized
5 Sat	25	10	1035	450	132.05	1.22	20.69	128.81	1.45	Localized
6 Dry	15		620	600	134.9	1.22	12.97	133.31	1.31	Localized
6 Sat	25	10	1035	600	103.19	1.1	11.69	100.96	1.2	Localized
7 Dry	30		1240	No	184.41	1.26	30.45	180.94	1.44	Localized
7 Sat	50	20	2065	No	127.25	1.44	20.78	127.25	1.44	Localized
8 Dry	50		2065	No			35.32		Ductile	Non-localized
8 Sat	84	34	3465	No			25.37		Ductile	Non-localized

AE output was recorded contemporaneously during each test on heating to, and cooling from 150 °C, 300 °C, 450 °C, and 600 °C. AE were recorded by using the central rods to act as acoustic waveguides with one Panametrics V103 piezoelectric P-wave transducer located at the end of the waveguide. The AE hits are used as a proxy for the rate and relative amounts of induced crack damage which includes indistinctively the nucleation, coalescence and propagation of newly-formed microcracks (assumed to be the most likely source here) as well as other microstructural processes susceptible to produce AE (such as friction between pre-existing microcrack's surfaces; Griffiths et al., 2018). A threshold of 35 dB was imposed on the recorded AE amplitude to avoid background noise (Browning et al. (2016)). All thermal treatment tests were conducted at ambient pressure (1 atm). Complementary ultrasonic P-wave and S-wave velocity measurements were recorded on the starting material prior to heating, and on the cooled material following each thermal stressing test.

### 3.3. Triaxial Deformation: Method and Data Collection

The experiments were performed using a conventional triaxial apparatus (where  $\sigma_1$  is the maximum principal stress,  $\sigma_2$  the intermediate principal stress and  $\sigma_3$  the minimum principal stress such that  $\sigma_1 > \sigma_2 = \sigma_3$ ; compressive stress is reckoned positive) capable of operating at a maximum confining pressure ( $P_c = \sigma_2 = \sigma_3$ ) of up to 100 MPa, and an axial stress ( $\sigma_1$ ) of up to 680 MPa across a 40 mm diameter cylindrical specimen (Figure 2b). An independent pore fluid system (using distilled water) was connected to the cell, which is capable of pressures up to 100 MPa via precision piston pumps (Fazio et al., 2017). Dry conditions were achieved by leaving the specimens in an oven at approximately 85 °C for 12 hours to avoid the presence of interstitial water, followed by cooling in a desiccator for 1 hour. Saturated conditions were achieved by immersing a subset of the specimens in distilled water under vacuum for 24 hours. Axial displacement during tests was measured by three contactless transducers (external Foucault current sensors) positioned on the frame of the apparatus, averaged and logged by a control computer at 1 Hz. The same data logger recorded pore and confining pressures as well as pore volumes to allow specimen dilation to be derived. Axial stress data were corrected for the stiffness of the machine using a calibrated aluminium specimen of known Young's modulus. We selected and applied a range of confining pressures ( $P_c$ : 7 MPa, 15 MPa, 30 MPa, and 54 MPa) simulating depths of 290 m, 620 m, 1.2 km, and 2.0 km respectively, assuming an average density of the overburden load of 2470 kg/m<sup>3</sup> (see Table 1).

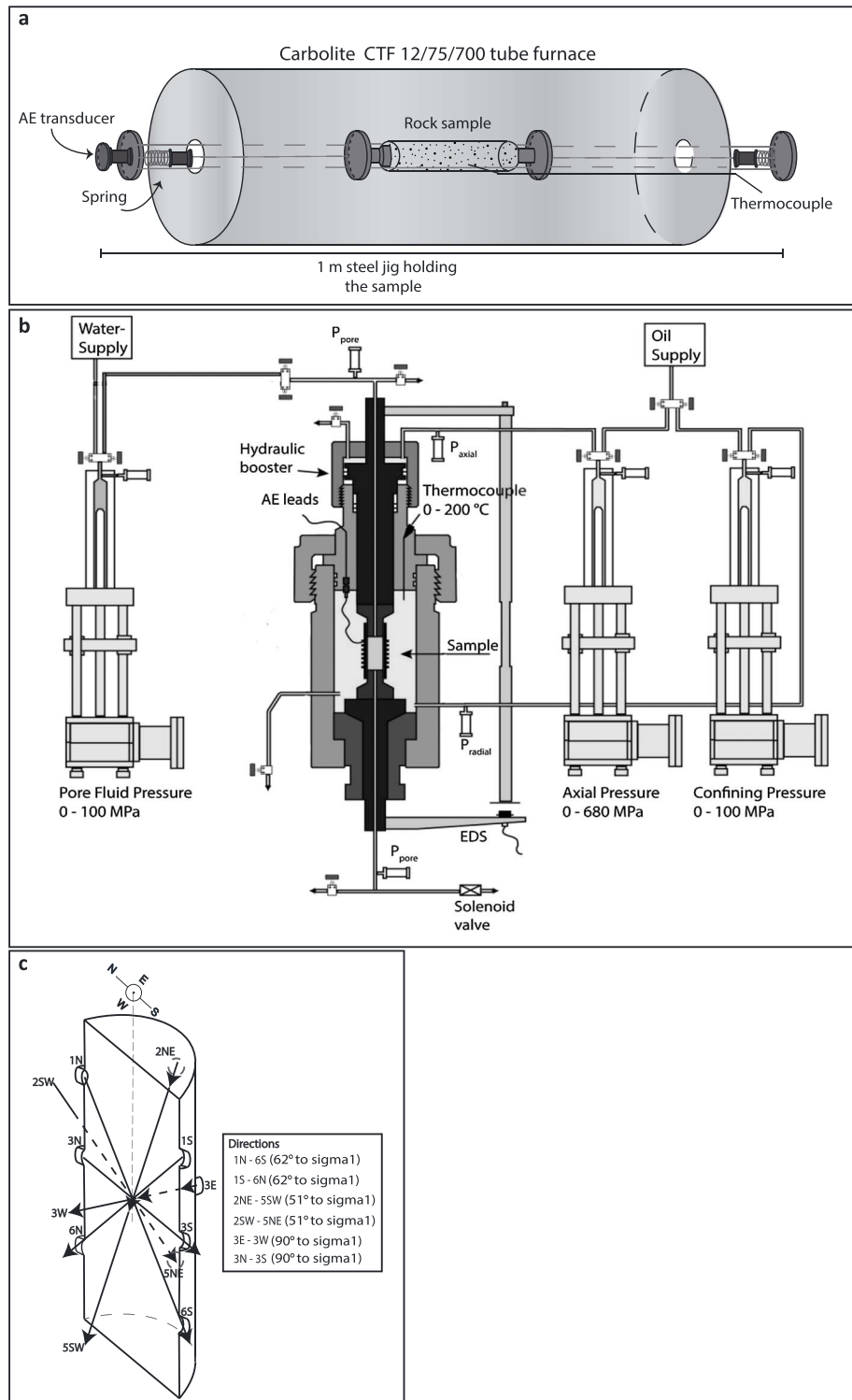


**Figure 2.** Schematic views of: a) the Carbolite furnace used to thermally treat specimens. The specimens is held within the Centre of the tube furnace, where the temperature remains constant. The two springs at the end of the jig allow contraction and expansion, registered by a transducer used for AE recording; b) the triaxial apparatus used; and c) the AE sensor positions and orientations around a half-specimen (originally 40 mm in diameter and 100 mm in length) in the arbitrary orientation system. The degrees are reported with respect to the maximum principal stress applied  $\sigma_1$  (i.E. in the vertical direction here).



Pore fluid pressures ( $P_f$ ) were calculated accordingly to represent the same depths and assuming drained conditions:  $P_f = 5$  MPa, 10 MPa, 20 MPa, and 34 MPa, respectively. To compare the dry and saturated data, we therefore maintain the same effective pressures applying a simple effective pressure law where the poroelastic constant  $\alpha$  is assumed to be equal to unity ( $P_{\text{eff}} = P_c - \alpha P_f$ ; Guéguen & Palciauskas 1994). In that common frame, a dry test at  $P_c = P_{\text{eff}} = 7$  MPa corresponds to a water saturated test where  $P_c = 12$  MPa,  $P_f = 5$  MPa and consequently  $P_{\text{eff}} = 7$  MPa. To investigate and isolate the role of temperature treatment,  $P_{\text{eff}} = 15$  MPa was maintained in all tests using thermally-treated specimens.

All tests were conducted at  $10^{-5} \text{ s}^{-1}$  axial strain rate in assumed drained conditions when relevant, and at room temperature. For saturated tests, the initial loading was applied in two steps, first by increasing  $P_c$  hydrostatically ( $\sigma_1 = \sigma_2 = \sigma_3$ ) until the desired confining pressure was reached, and then introducing pore fluid pressure, as per the functionality of our experimental set-up. We applied this method following Nicolas et al. (2016) who calculated the time of diffusion of water into a porous carbonate, concluding that for a quite significant porosity and standard axial strain rate (as used in our study) the specimens are fully saturated.

### 3.4. Ultrasonic Surveys

In addition to mechanical and pore volume data, the deformation was monitored using an array of 12 piezoelectric lead zirconate titanate (PZT) sensors embedded in an engineered nitrile jacket (Sammonds, 1999). These sensors are sensitive to transient fracture events (micro seismicity) across a frequency range of approximately 80 kHz to 800 kHz. In addition to the standard passive AE recording, each sensor can be excited in sequence with a 200 V pulse, recording the traveling signal on the remaining 11 sensors to deduce the elastic P-wave velocity structure of the specimen during deformation: This is known as a *velocity survey*. Signals from each sensor are pre-amplified by a Pulser Amplifier Desktop (PAD) unit by 60 dB before being sent to an AE recorder (ITASCA-Image "Milne" unit). Active P-wave velocity surveys are processed using the known location of each sensor (3 sensors along a selected north direction, 3 sensors along south, 2 at north-west and 2 at south-west, for a total of 12; Figure 2c), and the signal travel time from the source to each receiver (e.g. Benson et al., 2007; Fazio et al., 2017) determination of elastic anisotropy of the specimen during the application of differential stress. All ultrasonic data (passive AE and active velocity survey) are processed using the proprietary InSite-Lab software by cross-correlating a master pulse event with each received waveform, per survey, to achieve sub m/s (relative) accuracy.

## 4. Results

### 4.1. Thermal Treatment: Acoustic Emission and Ultrasonic Wave Velocities

Figure 3a shows the radial P-wave velocity ( $V_p$ ) of each specimen as a function of the increasing thermal treatment. Concentric reduction in specimen radial-velocities shows that the carbonate remained isotropic even after the thermal treatment, and that overall velocity decreased with increasing maximum temperature. 'As collected' CL specimen has a radial P-wave velocity of 4.60 km/s ( $\pm 0.17$  km/s) and are essentially isotropic (anisotropy  $< 4\%$ ). The change in P-wave velocity following the 150 °C thermal test is negligible and remains at approximately 4.60 km/s, overlapping the room-temperature specimen curve, therefore they are not reported here.

P-wave velocities decreased by approximately 5% to 4.26 km/s following heat treatment to 300 °C, and by 22% to 3.55 km/s, following heat treatment to 450 °C. Following the 600 °C thermal stressing test, P-wave velocities decreased by approximately 37% to 2.83 km/s (red line, Figure 3a). Figure 3b, c and d show AE outputs for tests heated to 300 °C, 450 °C and 600 °C. AE output was negligible in the 150 °C test and therefore is not reported. In tests performed to maximum temperatures of 300 °C and 450 °C, the AE output is similar in terms of amplitude (size of individual AE hits) and number of AE hits. In both cases the total amount of AE hits is low ( $< 1000$  events). Tests with a maximum temperature of 600 °C show substantial AE output (Figure 3C). The rate and amplitude of AE hits increased substantially at approximately 480 minutes and 500 °C in heating and continued to produce AE at a similar rate and size on cooling. The total AE hits recorded in the 600 °C test exceeds 1000 events.

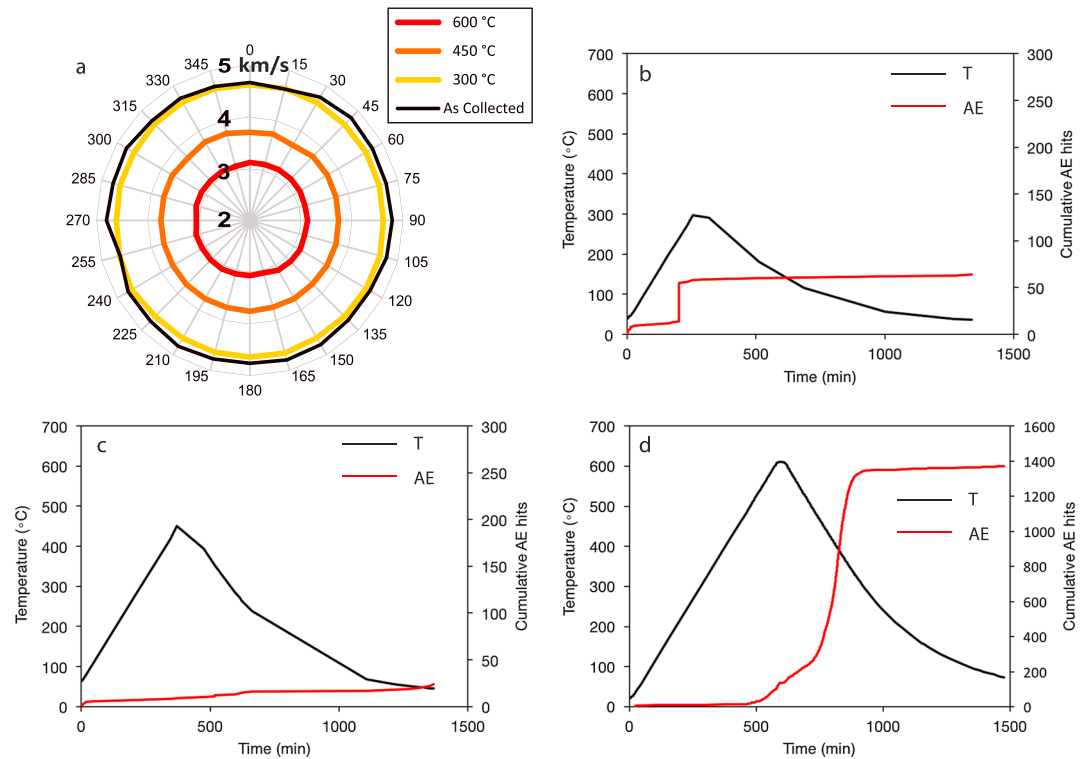


**Figure 3.** a) Radial ultrasonic P-wave velocities (km/s) as measured across the diameter of a cylindrical specimen at 15° increments. The thick black line represents the untreated (i.e., as-collected) specimen, reporting a P-wave velocity of 4.60 km/s. Lines represent the P-wave velocities as measured with increasing thermal temperature treatment. (b), (c) and (d) represent the contemporaneous acoustic emission output recorded during the thermal treatment at 300 °C, 450 °C and 600 °C respectively. Note the change of scale in cumulative AE hits in part d.

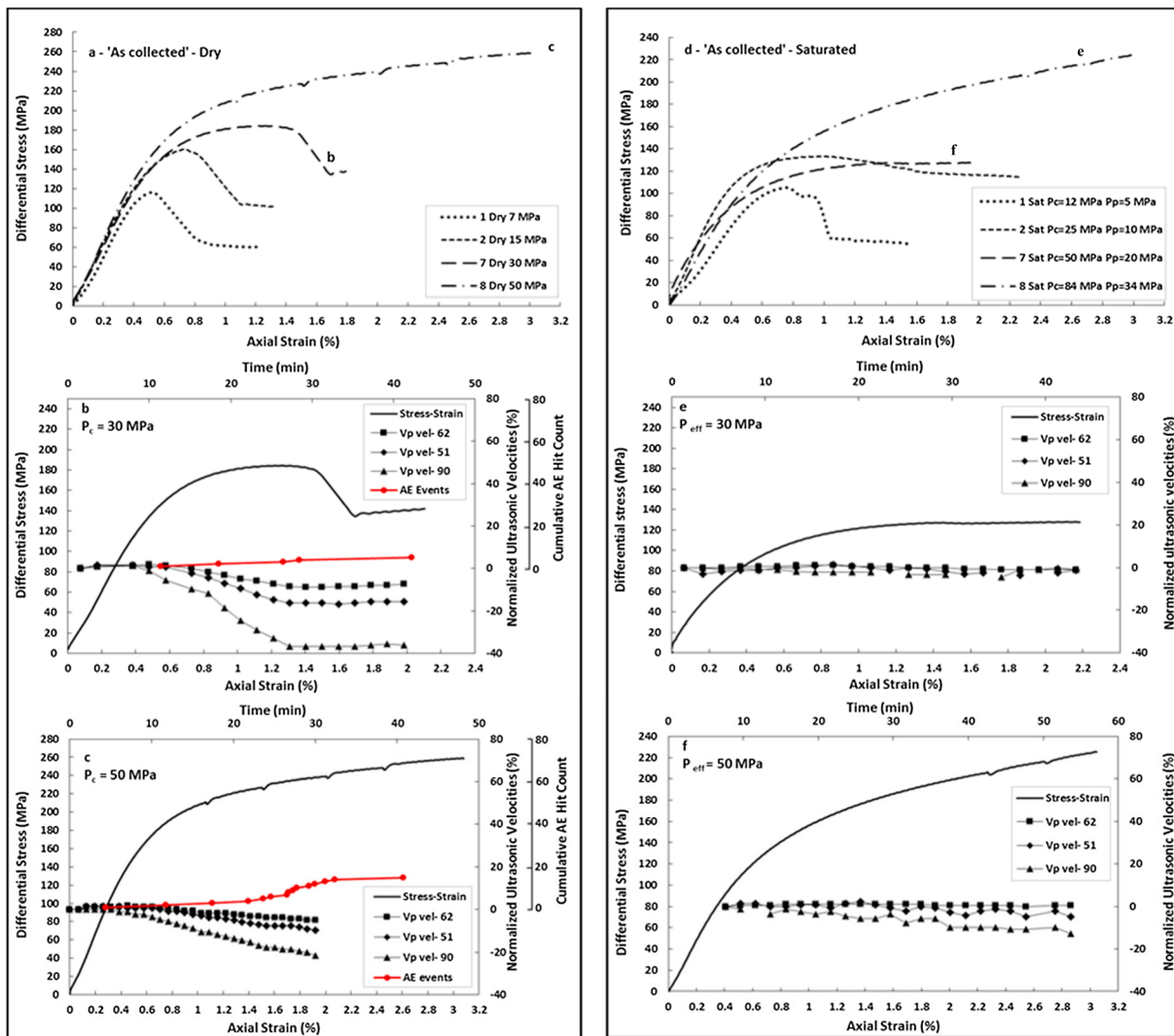
#### 4.2. Triaxial Test: Dry Conditions on ‘as Collected’ Specimens

Figure 4a shows the results from deformation experiments conducted on ‘as collected’ specimens of CL under dry conditions, at room temperature (22 °C), with increasing levels of  $P_{\text{eff}}$  (7 MPa, 15 MPa, 30 MPa, 50 MPa) representing increasing depth.

In the mechanical data we note a typical evolution from the brittle to the ductile regime as effective pressure increases beyond 30 MPa, with ductile behaviour clearly present at 50 MPa, defined as the capacity of the rock to undergo substantial strain without developing a microscopic fracture (Paterson & Wong, 2005) or loss of strength (Bakker et al., 2015). The two tests conducted at 50 MPa confining pressure exhibit small ‘bumps’ in the stress–strain curve. These represent steps of increasing confining pressure (each of 5 MPa). In all cases and across higher effective pressures, the specimens attained substantial strain without the development of a macroscopic shear fracture. All tests show an initial stage of strain hardening due to the closure of pre-existing cracks and/or pores (e.g. Baud, Schubnel, & Wong, 2000; Nicolas et al., 2016) followed by linear elastic behaviour. Experiments 1, 2 and 7 (all dry) attained a peak stress at 116.23 MPa, 160.59 MPa and 184.41 MPa, respectively followed by strain softening and brittle failure (Figure 4a and Table 1). To better understand the accommodation of deformation at the brittle to plastic (BP) transition, Figures 4b and 4c additionally plot the detail of experiment 7 (Dry, 30 MPa) and experiment 8 (Dry, 50 MPa). Normalized  $V_p$  and cumulative AE hit rates have been added to better understand the strain accommodation.

At  $P_c = 30$  MPa (Figure 4b), the  $V_p$  velocities increase as well, up to 1.52% at 0.2% axial strain. Then, they start to decrease at the onset of inelastic deformation (0.4% axial strain), leading towards failure where the velocities reach a minimum. The most marked decreases in velocity are in the 3 N-3S and 3E-3 W directions, both at 90° respect to  $\sigma_1$ , corresponding to the directions traveling through the centre of the specimens. After failure velocity remains steady at between –8 to –35% below initial values; this directional variation in  $V_p$  represents a significant anisotropy. AE cumulative hit rate increased steadily during deformation and strain





**Figure 4.** (a-b-c). Triaxial test results in dry conditions, for non-thermally-treated specimens. (a) Differential stress versus axial strain, as a function of increasing confining pressure (see inset key). (b) and (c) are stress-strain plots with corresponding, normalized, ultrasonic velocities along three representative directions, and cumulative AE hit count (red line) for the test conducted at (b) 30 MPa and (c) 50 MPa effective pressure. Figure 4 (d-e-f) are the triaxial test results in drained, saturated conditions, for non-thermally-treated specimens. AE hit count is not reported as the event rate was too low. In the final tests (Figure 4c and f),  $P_c$  was increased in steps of 5 MPa after 1% and 2.2% strain, respectively, in an attempt to check for changing behaviour in the ductile response as a function of burial depth, using the same experimental setup. The increasing  $P_c$  steps result in small differential stress ‘bumps’ in the stress-strain curves.

accommodation, showing a marked increase from the time of stress drop (dynamic failure), although only a small number of AE events were recorded.

At 50 MPa of  $P_c$  (Figure 4c), we observe a ductile behaviour, setting the BD transition somewhere between 30 and 50 MPa. The elastic-wave velocity data shows a path dependence with direction. An initial increase up to 1.55% in the direction at 62° and 51° to  $\sigma_1$  at 0.2% axial strain, whereas there is no increase for the ray-path at 90°. For the first two ray-paths the velocity starts to decrease after the elastic accommodation reaches a value of -5% and -10%, respectively. The ray-path at 90° shows a continuous decreasing velocity to a minimum of -21.7%. The  $V_p$  velocities represent a lower anisotropy than tests at 30 MPa  $P_c$ . Cumulative AE data show a slow increase initially, which accelerates towards the end of the experiment.

### 4.3. Triaxial Test: Drained Saturated Conditions on ‘as Collected’ Specimens

Figure 4d presents data in drained saturated conditions. There are several notable differences in stress and strain accommodation compared to tests in dry conditions. Experiment 1 and 2 Sat attain a peak stress at 105.09 MPa, 0.76% axial strain, and at 133.49 MPa, 1.01% axial strain respectively followed by strain

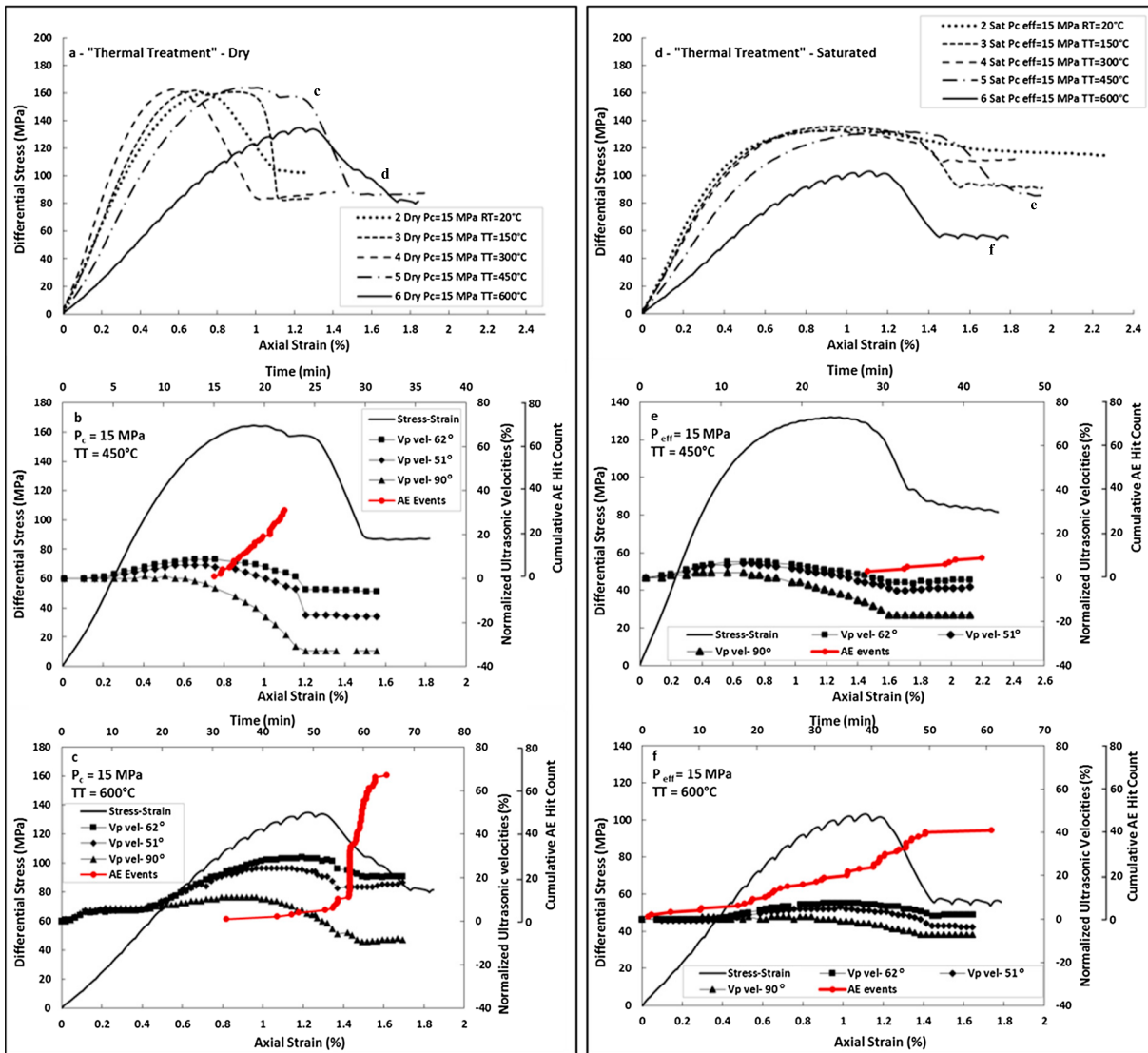


**Figure 5.** (a-b-c). Triaxial test results in dry conditions for thermally-treated specimens, at a constant 15 MPa effective pressure. (a) Differential stress versus axial strain, as a function of maximum thermal treatment temperature (see inset key). (b and c) Stress–strain plots with corresponding, normalized, ultrasonic velocities along three representative directions, and cumulative AE hit count (red line) for the test conducted on specimens treated to (b) 450 °C and (c) 600 °C. Note the initial increase in ultrasonic velocities in c) across all raypaths likely indicating thermal induced micro-cracking, followed by velocities reduction corresponding to an increase in AE hit count. Figure 5 (d-e-f) are the triaxial test results in drained, saturated conditions for thermally-treated specimens, at a constant 15 MPa effective pressure.

softening. The peak stresses are lower (between 5% and 20% MPa less) compared to dry conditions at equivalent effective pressure (cf. Figure 4a and Table 1). Young’s modulus is also lower in saturated conditions (Table 1), and in general there is significantly more total strain accommodation before failure (such as the case of  $P_{eff} = 7$  and  $P_{eff} = 15$  MPa). At  $P_{eff} = 30$  MPa, the specimen accommodates strain hardening up to 1.5% axial strain, where a small stress drop is recorded. At 50 MPa the specimen is dominated by ductile deformation. The BD transition is again between 30 MPa and 50 MPa  $P_{eff}$ . AE are not reported for the experiments in Figures 4e and 4f, as the number of events were negligible.

The transition from brittle to ductile behaviour along with normalized  $V_p$  are reported in Figure 4e and Figure 4f using data from experiment 7 Sat ( $P_{eff} = 34$  MPa) and experiment 8 Sat ( $P_{eff} = 54$  MPa) respectively. At  $P_{eff} = 30$  MPa the behaviour is characterized by strain hardening until brittle failure but the stress drop is barely discernible at around 1.5% strain. Post-mortem macroscopic inspections revealed the presence of wedge splitting along with several conjugate fractures (see supporting material). The P-wave elastic

velocity data remain essentially constant throughout the experiment. The level of velocity anisotropy is low, with a range from  $-1\%$  to  $-5\%$  velocity decrease towards the end of the experiment.

At higher  $P_{\text{eff}} = 50$  MPa (Figure 4f), the divergence from elastic to plastic behaviour starts at 70 MPa differential stress or 0.3% strain, about 20 MPa less than the data reported in Figure 5a. Similar trends are seen with regards to  $V_p$  with in general a small continuously decreasing trend in the data for the velocities at  $62^\circ$  and  $51^\circ$  to  $\sigma_1$  finally resulting in anisotropy values ranging between 0% and  $-5\%$ . The ray-path traveling perpendicular to  $\sigma_1$  is the most affected and decreases by 13%. The overall anisotropy is lower than the anisotropy recorded in the dry test (i.e. 8 Dry, Figure 4c).

#### 4.4. Triaxial Tests: Dry Conditions on Thermally Treated Specimens

Figure 5a shows mechanical results from triaxial experiments run at room temperature on previously thermally-treated CL. Here, a constant confining pressure was maintained at 15 MPa so as to investigate only the influence of the heat treatment, ranging from untreated (as collected) to 600 °C. All the specimens reached the same peak stress (160–162 MPa) before failure regardless of thermal treatment temperature with the exception of the specimen at 600 °C, which failed at 138 MPa peak stress. The stress–strain curves remain similar until treatment of approximately 450 °C. At 600 °C the behaviour starts to be weaker and in fact the Young's modulus is markedly lower compared to specimens treated at lower temperatures (see Table 1). The trend in total strain at failure is likewise tied to the thermal treatment temperature, with a tentative increase in the percentage strain at failure with increasing thermal treatment, but a clear behavioral variation is observed beyond 450 °C. Conversely, the stress drop itself appears to be constant (between 60 to 80 MPa) with the thermal treatments.

Figures 5b and 5c show detail of normalized  $V_p$  and AE hit rates for the highest thermal treatment of 450 °C and 600 °C experiments. For experiment 5 Dry (450 °C), the initial strain accommodation is followed by elastic accommodation until approximately 80 MPa, 0.3% axial strain. After the peak stress occurring at 0.9%, the specimen enters a strain softening phase, with a complex strain softening behaviour. In comparison to the 'as collected' specimens where ultrasonic velocities show a small increment at the beginning of the experiments, here  $V_p$  data shows an overall trend of higher velocities for the dry experiments prior to failure. For the 450 °C treated specimen, velocity data indicates a significant velocity anisotropy developing prior to failure, with velocities ranging from  $+8\%$  to  $-4\%$ . The most affected ray-path once again was at  $90^\circ$  to  $\sigma_1$  which suggests the formation of axial fractures opening perpendicular to  $\sigma_1$ . For the specimen treated to 600 °C the behaviour appears similar. However, specimen strength is affected by the prior thermal treatment. In the specimen treated to 600 °C the peak stress occurred at 1.22% axial strain and 134 MPa differential stress compared to the specimen treated at 450 °C where the peak stress occurred at 0.94% axial strain and 164 MPa differential (Figure 5c). In both cases the specimen developed a localized shear fracture. Also, in both cases, AE hit rate starts to increase dramatically when approaching the peak stress and failure, with a supra-exponential trend evident for the specimen treated to 600 °C, whilst the specimen treated to 450 °C has a more linear trend.

#### 4.5. Triaxial Tests: Drained Saturated Conditions on Thermally Treated Specimens

Figure 5d shows the stress versus strain results for thermally-treated specimens in saturated, drained conditions. Peak stress is lower across all specimens (about  $-30$  MPa in all the experiments) compared to dry deformation (cfr. Figure 4d and Table 1), and is very similar (approximately 132 MPa) to the lowest three thermal stressing temperatures (20 °C, 150 °C, 300 °C); stress–strain paths are virtually identical with a maximum strain at failure of approximately 1.4%. Saturated conditions for the thermal treatment at 450 °C shows an increase in strain at failure to approximately 1.5% and a slightly lower peak stress of 130 MPa. The presence of pore fluid pressure along with the thermal treatment at 600 °C resulted in a significant change in peak stress and stress–strain path, with strain at failure of 1.2% and peak stress of 100 MPa. In all cases the strain accommodated before the peak stress and before failure is significantly increased relative to tests in dry conditions (Figure 5a). Specimens show a systematic decrease in the static Young's modulus with increasing thermal treatment temperature. Focusing on the transition from 450 °C (Figure 5e) to 600 °C (Figure 5f), in both experiments an initial increase in  $V_p$  is recorded followed by a decrease, occurring at approximately 0.8% strain for 450 °C and approximately 1% for 600 °C. As was the case for dry experiments, the normalized velocity increases initially with deformation from 0% to  $+7\%$  in both cases, and ultimately giving anisotropy values ranging from  $-4\%$  to  $-16\%$  (450 °C) and  $+2\%$  to  $-10\%$  (600 °C). For experiment 5 Sat (450 °C) AE

cumulative hit rate shows few events before yield and failure whereas the AE hit rate for experiment 6 Sat (600 °C) shows a significant AE hit count compared to the previous experiment from the beginning of the deformation, which increases discontinuously until the stress drop occurs.

## 5. Discussion

### 5.1. Mechanical Behaviour of Dry and Saturated Specimens 'as Collected'

For dry, 'as collected' specimens it is evident that a classical brittle to ductile behaviour starts to evolve when crossing a threshold confining pressure of approximately 30 MPa. The transition we observe is a steadily flattening and widening pre- and post-peak behaviour in the stress–strain curve. For dry experiments at 30 MPa, the amount of strain accommodated at peak stress is 1.26%, considerably higher than that at 15 MPa (at 0.73%). At 50 MPa the behaviour is in ductile regime. The experiment shows that strain hardening is generally insensitive to confining pressure increases (the jumps in the differential stress due to  $P_c$  increase). Bakker et al. (2015) showed that for CL at 50 MPa confinement and  $10^{-5} \text{ s}^{-1}$  strain rate, the specimen reached peak stress at 370 MPa of differential stress sustaining 1.8% axial strain, with strain softening behaviour before failure. However, reviewing the specimen descriptions of Bakker et al. (2015) it is evident that their study used a more dolomitic material, compared with our calcite CL specimens. At the same confining pressure our specimens were already within the ductile regime. Nicolas et al. (2016) conducted dry experiments on Tavel Limestone, at the same constant axial strain rate and room temperature, which exhibited brittle behaviour for confining pressures up to 55 MPa. They found that for  $P_c \geq 70$  MPa the behaviour changed to a semi-brittle regime, defined as a coupled plastic deformation and induced damage (Evans et al., 1990). In our experiments the brittle-ductile transition is found to occur at confining pressures above 30 MPa, for specimens tested at room temperature and without thermal treatment. This is likely due to the larger grain size of CL compared to Tavel limestone (see Nicolas et al., 2016 and Vajdova et al., 2004, 2010 for more details about Tavel limestone). As porosity and grain size increase, the brittle to cataclastic flow transition can occur at lower confinement (Wong & Baud, 2012).

In saturated conditions, Nicolas et al. (2016) the failure behaviour of the Tavel limestone in the brittle and semi-brittle regime. However, water did have a weakening effect lowering the peak stresses at which dilatancy occurred. In our water-saturated experiments, the response of CL changes at  $P_{\text{eff}} < 30$  MPa. Water lowers the mechanical strength, decreasing peak stresses and promoting strain softening as seen for experiments 1 and 2 Sat (Figure 4d). Baud, Zhu, and Wong (2000) explained the reduction of sandstone brittle strength in presence of water integrating the Orowan's generalization of the Griffith-Irwin equilibrium concept (e.g. Lawn, 1993) in a sliding wing crack model. Since we recorded AE during the deformation of our saturated samples, we can assume that most of the brittle damage measured was controlled by micromechanisms at the grain-scale too. Water molecules could have lower the microcrack interface energy on entering and adsorbing onto the walls in the cohesion zones, diminishing the stress intensity in our saturated limestone samples compared to the dry ones. Experiment 7 Sat at  $P_{\text{eff}} = 30$  MPa undergoes strain hardening until the deformation localizes, resulting in wedge splitting and conjugate fractures localized in the upper part of the sample. At  $P_{\text{eff}} = 50$  MPa the behaviour of CL (experiment 8 Sat) is in the ductile regime, presenting strain hardening insensitive to increasing confining pressures (Figure 4f). As highlighted by previous studies, ultrasonic wave velocities and AE are both sensitive to inelastic damage, what can be crack nucleation and/or propagation under sufficiently high differential stresses (Browning et al., 2017 and reference therein).  $V_p$  velocities are decreasing as crack damage is increasing. The behaviour of the recorded ultrasonic velocities for our experiments (Figure 4b-c-e-f), is reflecting the previous findings. The  $V_p$  velocities increase at the beginning of the tests when differential stress is applied, during closure of pre-existing micro-cracks (Browning et al., 2017). The change in velocities at the onset of inelastic accommodation depends on the direction of the considered ray-paths. In general the most affected direction showing the higher anisotropy is the ray-path at  $90^\circ$  to  $\sigma_1$ , where travel is across newly-generated fractures. Encountering a high density of microcracks is increased with a high incidence angle, as consistently demonstrated in our data, and in common with other studies (Harnett et al., 2018).

### 5.2. Effects of Thermal Treatment on Comiso Limestone Strength

In our experiments, pre-deformation thermal treatment is seen to have an influence on the rock mechanical properties. XRPD analyses on powders of specimens treated at 600 °C revealed the presence of Portlandite.

As reported by Heap et al. (2013), Portlandite is a calcium hydroxide which is the result of the combination of CaO (product of decarbonation) with water in the atmosphere after the thermal treatment, according to the formula  $\text{CaO} + \text{H}_2\text{O} = \text{Ca}(\text{OH})_2$ . As this is an exothermic reaction, it provokes an increase in volume, affecting the specimens even further (no measures of volumes are available here). Decarbonation has been reported to be one of the cause of weakening in strength (Heap et al., 2013; Mollo et al., 2011). A collection of SEM images of our thermally treated specimens is in Figure S2 (supplementary material) showing the increased porosity. Amongst the results found by Heap et al. (2013), a few comparisons can be made between CL and MCL (Monte Climiti Limestone - 100% calcite). In Uniaxial Compression tests, the MCL specimens that were previously thermally treated up to 800 °C, showed no variation in strength up to 500 °C, with a peak stress at 0.3% axial strain ( $1.0 \times 10^{-5} \text{ s}^{-1}$ ). For  $500^\circ\text{C} < T < 650^\circ\text{C}$ , the strength showed no variation but the specimens attained the peak stress at 0.6% axial strain. As Heap et al. (2013) highlighted, the addition of  $P_c$  results in a reduction of the temperature required to switch to a ductile flow. Bakker et al. (2015) and Nicolas et al. (2016) performed triaxial experiments on CL and Tavel Limestone respectively, and both also applied room to *in situ* temperatures while deforming. Bakker et al. (2015) found the Young Modulus to be insensitive of  $P$ , but sensitive to  $T$ , decreasing from 34 GPa at 20 °C to 16 GPa at 600 °C. Our tests show a decrease from 28.7 GPa at 20 °C to 12 GPa in the samples pre-treated at 600 °C. Nicolas et al., 2016 conducted experiments of Tavel Limestone at 70 °C, finding an overall reduced strength, but with the brittle to semi-brittle transition occurring at a lower confinement: between 35 and 55 MPa, in dry conditions. Conversely, the experiments run at  $P_c = 50$  MPa of Bakker et al. (2015), showed a BD transition at  $350 \pm 50$  °C. The data we report, although at different pressure and temperature conditions, support the idea that the presence of elevated temperatures can impress limestone microstructure (thermal damage) by lowering its mechanical strength; this is true either when elevated temperatures are present during mechanical deformation or when elevated temperatures were present before.

In our experiments, the pre-test thermal treatment illustrate an underlying thermal damage that is only partially characterized by AE output: at 150 °C CL does not show any significant AE output or damage, supported by unchanged P-wave velocities. Low AE counts in the 300 °C – 450 °C thermal stressing tests would also, apparently, indicate the absence of significant damage, however P-wave velocity decreases by up to 17% over this temperature range (Figure 3 a,b,c), indicating indeed that thermal damage is present. We interpret that these temperatures do induce thermal damage but likely the low AE output is likely indicative of the natural variability of this rock. At 600 °C (Figure 3 a and d), the number of AE increase dramatically along with a consistent  $V_p$  decrease. At this temperature, different mechanisms of thermal damage might be activated, such as decarbonation and quartz  $\alpha$  to quartz  $\beta$  transition (573 °C, ambient  $P$ : Tuttle, 1949) the latter corresponding to increasing volume. Elastic P-wave anisotropy measurements further confirm the development of a pervasive fracture damage that is extended and promoted by the thermal treatment. Regarding the results obtained during the triaxial tests at room temperature, given the consistent nature of the peak strength of the thermally treated materials, it is thought that the previous heat treatment promoted inter-granular cracking (e.g. Fredrich & Wong, 1986) that locks the overall specimen to give a consistent strength, but with additional heating, allows a higher total strain at failure, as seen in the data (Figure 6). This influence extends in dry and saturated conditions, where the strength is at 160 MPa, between 0.57% and 0.91% axial strain and 130 MPa and 0.67% to 1.22% axial strain, respectively. Whilst the anisotropy reaches a maximum of 15% (span ranging from –3% to –18%) for dry untreated specimens, this increase to 30% (span +10% to –20%) after thermal treatment to 600 °C. The effect is subdued when water is present, increasing from 10% (0 to –10) to 17% (+7 to –10) due to thermal stressing, with the lower anisotropy providing further evidence of crack fabric, but this time filled with pore fluid that seeks to lower the effective elastic wave speed (e.g. Mavko et al., 1998). The AE trend shows indeed an increment in the final output for the thermally treated specimens, whereas for the as collected specimens the trend is slightly flat and homogeneous throughout the experiments. Overall, with respect to the previous triaxial experiments run with *in situ* temperature, our previous thermal treatment assumes a different point of view. An *in situ* experiment aims to reproduce either a condition in depth or the presence of a magmatic body close to the rocks at the same time of the deformation. Triaxial tests at room temperature run on specimens previously treated and at modest confining pressures representing depth, aims to reproduce a common situation in volcanic environment: the intrusion of magma bodies which bring to the deterioration of the country rocks. Being deteriorated, these rocks will be more prone to fail and accommodate structural deformation which are of fundamental importance in the overall stability of the edifice.



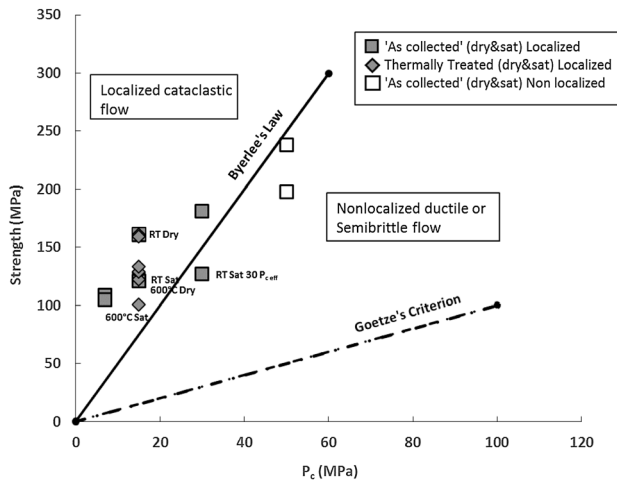


**Figure 6.** Experimental results plotted on a strength vs  $P_c$  plot.

### 5.3. Brittle-Ductile Transition

To provide a macroscopic description of the brittle-ductile transition, the data from all of our tests were plotted in strength vs  $P_c$  space (Kohlstedt et al., 1995) (Figure 6). For those experiments that produced ductile behaviour we measured the strength consistently at a threshold of 2% axial strain. Byerlee's Rule (black line) and the Goetze's Criterion (dotted line) are reported as they delimit the brittle region from the semi-brittle region (Figure 6).

We find that most of the experiments concentrate in the brittle region which is characterized by localized cataclastic flow. We highlight in Figure 6 the two end-member thermal treatment cases, RT (room temperature) and 600 °C both under dry and saturated conditions. The specimen treated to 600 °C has a strength comparable to that of the saturated RT specimen indicating that both water and thermal cracking have a strong influence on strength. We also highlight the experiment under saturated conditions at  $P_c = 30$  MPa, which exhibited a strain hardening behaviour typical of the semi-brittle regime but which eventually

reached failure (Figure 6). The two experiments that induced ductile behaviour fall in the transitional region, as confirmed from the macroscopic inspection of the post-mortem specimens. According to Evans and Kohlstedt (1995), these experiments transition to a failure mode from localized to ductile, into the mechanism class from brittle to semi-brittle, involving both plastic and brittle mechanisms. Our results explore only a single strain rate whilst the sensitivity of rock strength to strain rate is known to be very pronounced in the semi-brittle and ductile domain, especially in presence of continuous high temperature and/or creep conditions.

### 5.4. Application of Results to the Etna Basement

At Mount Etna previous studies have located the presence of shallow magma reservoirs between 3–5 km depth, within the sedimentary basement (Aloisi et al., 2011; Bonaccorso, 1996; Bonaccorso et al., 2010; Gambino et al., 2016): this provides one of the key motivations for this study. Magmatic intrusions generate high temperature gradients, which can have a significant effect on the mechanical, chemical, and physical properties of the surrounding rocks, especially sedimentary rocks which are more prone to the effect of temperature and fluids circulation, promoting micro-cracking development and enhancing inelastic behaviour (Heap et al., 2013; Mollo et al., 2011; Nicolas et al., 2016; Rutter, 1972, 1974; Yavuz et al., 2010). As carbonate rocks have a tendency to exhibit ductile behaviour already at laboratory temperature and strain rate (Baud, Schubnel, & Wong, 2000), the addition of fluids, and the thermal cracking effect, as shown here, will lead to ductile behaviour in the sedimentary basement. Magma reservoirs in the Etna's sedimentary basement feed both central and lateral conduits as well as numerous dykes and sills (Aloisi et al., 2011; Bonaccorso et al., 2010; Bonforte et al., 2008; Gambino et al., 2016). In general, dykes at Etna can be classified into two main types: a) horizontally propagating dykes that originated from a central conduit to the point of eruption (Sigmundsson et al., 2010) and b) vertically propagating dykes fed from a shallow magma reservoir which bypass the central conduit and intrude through the entire basement towards the surface. This latter type is the more typical for the Etna's basement (Aloisi et al., 2009; Bonaccorso et al., 2010; Gambino et al., 2016; Gudmundsson, 2002). The volume of sedimentary substratum that is thermally affected by shallow magma reservoirs (3–5 km depth) at Mount Etna is approximately 6 km<sup>3</sup>, with a temperature gradient from 1200 °C to 300 °C at a radial distance of 1.5 km (Mollo et al., 2011 and reference therein). Magmatic intrusions, whether dykes or sills, or sub-spherical pressure sources, produce substantial heat which likely affects the basement rocks of Mt Etna, and other volcanoes with sedimentary substratum. To relate our laboratory data to a physical model considering the proximity to a dyke intrusion, we constructed a 2D finite element model using COMSOL Multiphysics (Figure 7).

Here, we consider the thermal effects on a carbonate host rock from the intrusion of a vertical basaltic dyke with a temperature of 1200 °C (Figure 7a). Using the heat transfer module in COMSOL, we build an axisymmetric 2D representation of a 1 m and 10 m thick dyke intruding into a cooler carbonate host rock with an average calcite thermal conductivity ( $k_c$ ) of 2.5 W K<sup>-1</sup> m<sup>-1</sup>, and a base temperature of 50 °C (Figure 7a). A finite element mesh is created around the intrusion with a maximum resolution of 0.5 m. The model then solves the



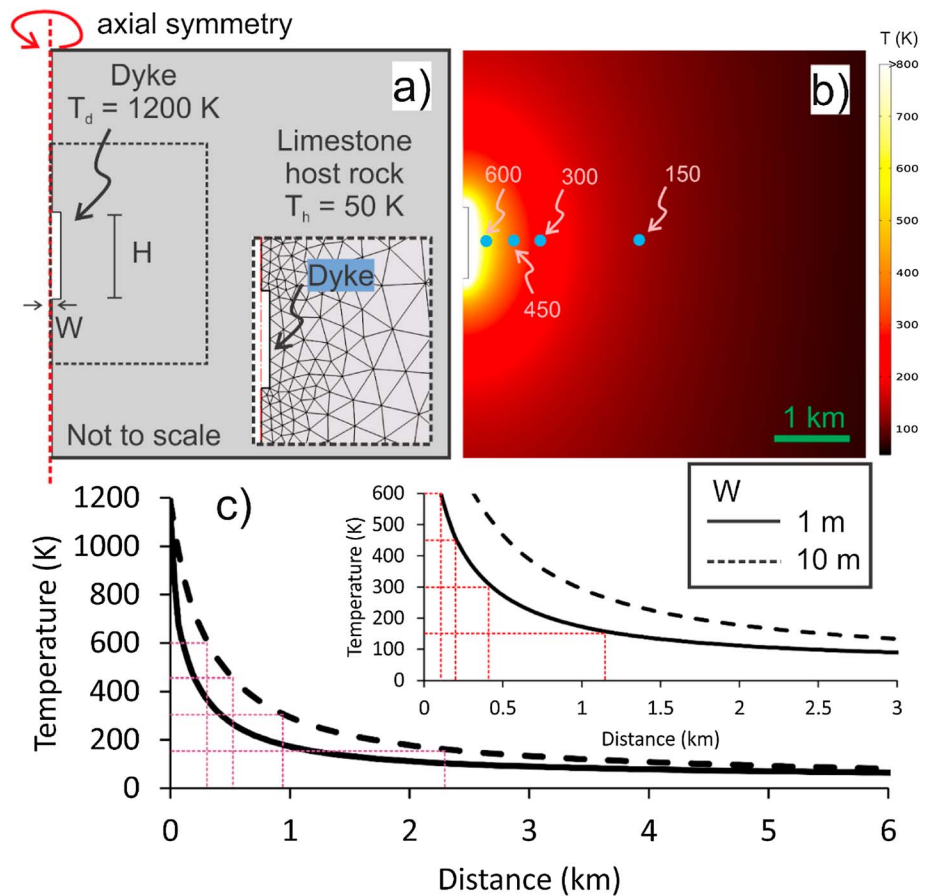


**Figure 7.** 2D finite element model representing a dyke as heat source (of 1200 °C) embedded in a cooler carbonate host rock (of 50 °C). (A). Model set-up and parameters. (B) Model results showing temperature decay away from a 1 m thick dyke. (C) Temperature versus distance plot for a 1 m thick dyke, and for a 10 m thick dyke. Inset shows zoomed view up to 600 °C, for a distance up to 3 km. Thin dashed lines show representative temperatures as per the thermal treatment experiments. Data are summarized in Table 2.

heat transfer equation (1) for conduction throughout the 20 km<sup>2</sup> domain to calculate the resultant temperature field of the host rock following intrusion (Figure 7b) as follows:

$$\rho C_p \Delta T + \Delta \cdot (-k \Delta T) = Q \quad (1)$$

where  $\rho$  is density,  $C_p$  is specific heat capacity and  $Q$  is heating power per unit volume. This is a first order model that calculates the instant temperature field ( $\Delta T$ ) in an isotropic dry host rock and so does not consider time dependant effects or preferred pathways for convective heat transfer or fluid rock interactions. The model therefore does not fully characterize the complexities of a thermal regime surrounding an intruded dyke but instead provides insights of the effect of temperature with proximity to a heat source. Applying this model to the heat-treated laboratory specimens suggests the expected approximate distance from the two different thicknesses of dykes that each specimen represents. In the case of a 1 m thick dyke intrusion, our four heat treated specimens represent a proximity to the dyke of 0.1 km at 600 °C, 0.2 km at 450 °C, 0.43 km at 300 °C, and 1.2 km at 150 °C. For a dyke of 10 m thickness, which is an extreme case for Etna, but commonly found at other volcanoes (e.g., Gudmundsson, 1995), the temperature field is much hotter which is entirely as expected. Increasing dyke thickness reduces the temperature decay at distance from the heat source: for a 10 m dyke, the 600 °C heat treatment would now be experienced at 0.3 km, 450 °C at 0.5 km, 300 °C at 0.95 km and 150 °C at 2.5 km from the dyke (Table 2).

Although being a quite simple model, when combined to laboratory analysis, one can observe that a dyke 1 m thick can already exert a critical influence on the mechanical properties of CL present a few hundreds

**Table 2**  
Modeled Proximity to a Dyke of Each Thermally Treated Sample

Dyke thickness (m)	Proximity to dyke (km)	Temperature (°C)
10	0.3	600
10	0.5	450
10	0.95	300
10	2.5	150
1	0.1	600
1	0.2	450
1	0.43	300
1	1.2	150

of metres away, and that this scenario may easily be extended across the depths where dykes and limestone are present in situ.

## 6. Conclusions

We have conducted a new series of experiments on Comiso limestone (CL) specimens. This study investigates the strength and strain accommodation dependence of the carbonate related to proximity to magmatic bodies and the presence of pore fluid, both as a function of burial depths (pressure) and fracture damage. Medium and high temperature were used to create thermal damage in the specimens prior to the mechanical testing to mimic the thermal stress of a distant heat

source or the influence of a “recently cooled” magma body into the host carbonate rock. Based on our results, we conclude that even a modest temperature of 450 °C can affect the carbonate strength, which is relevant for the units present in the substratum underlying Mount Etna. At 600 °C does CL definitely become weaker, so below the decarbonisation point. Our triaxial experiments confirmed that CL does not generate significant acoustic emissions, at least up to 450 °C of thermal treatment. However, a substantial development of new micro-cracks between 300 °C to 450 °C has been detected by the recording of ultrasonic wave velocities after the thermal treatment, which decreased from 4.26 km/s to 3.55 km/s and up to 2.83 km/s at 600 °C. Additionally, our study highlights that the marked decrease in mechanical strength of CL either due to thermal damage or the presence of water (pore fluid) enhances inelastic strain accommodation without dynamic failure by promoting the brittle-ductile transition regime of deformation at shallower depths. Finally, even if beyond the primary scope of our study, our modeling results indicate that the critical aseismic temperature zone in relation to the CL unit is likely to extend as far away as 2.5 km away from a 10 m thick dyke, a distance encompassing a large thickness of sub-Etnean pile if applicable, thus suggesting a very ductile substratum. In any case, our study presses the need to better assess the deformation of volcanic basements, with wide applications to other tectonic settings (as for instance the Campi Flegrei, Italy) and geothermal and reservoir fields.

## Acknowledgments

The authors thank Emily Butcher for technical assistance in the laboratory and for specimen preparation, and Pete Rowley for fruitful discussions and data processing assistance; Cheryl Haydon and Tom Knott from Leicester University for the training in XRPD and XRF techniques, Vinay Patel, Advanced Microscopy Centre Manager at Engineering Dept in Leicester. The authors are grateful to the Editor Andre Revil and reviewers Mike Heap, Marie Violay and the third reviewer for their comments which significantly helped to improve this manuscript. AC and SV acknowledge Project ‘SAFER’, EU grant FP7-PEOPLE-2013CIG n. 618346. PB acknowledges funding from the Royal Society (equipment grant) number RG130682. AOS is very grateful to the British Geological Survey science programme for all the support. Users can access the data used in the paper via the supplementary files.

## References

- Aloisi, M., Bonaccorso, A., Cannavò, F., Gambino, S., Mattia, M., Puglisi, G., & Boschi, E. (2009). A new dyke intrusion style for the Mount Etna may 2008 eruption modelled through continuous tilt and GPS data. *Terra Nova*, 21(4), 316–321. <https://doi.org/10.1111/j.1365-3121.2009.00889.x>
- Aloisi, M., Mattia, M., Ferlito, C., Palano, M., Bruno, V., & Cannavò, F. (2011). Imaging the multi-level magma reservoir at Mt. Etna volcano (Italy). *Geophysical Research Letters*, 38, L16306. <https://doi.org/10.1029/2011GL048488>
- Bakker, R. R., Violay, M. E. S., Benson, P. M., & Vinciguerra, S. C. (2015). Ductile flow in sub-volcanic carbonate basement as the main control for edifice stability: New experimental insights. *Earth and Planetary Science Letters*, 430, 533–541. <https://doi.org/10.1016/j.epsl.2015.08.017>
- Baud, P., Schubnel, A., & Wong, T.-F. (2000). Dilatancy, compaction, and failure mode in Solnhofen limestone. *Journal of Geophysical Research*, 105(B8), 19,289–19,303. <https://doi.org/10.1029/2000JB900133>
- Baud, P., Zhu, W., & Wong, T. F. (2000). Failure mode and weakening effect of water on sandstone. *Journal of Geophysical Research*, 105(B7), 16,371–16,389. <https://doi.org/10.1029/2000JB900087>
- Benson, P. M., Thompson, B. D., Meredith, P. G., Vinciguerra, S., & Young, R. P. (2007). Imaging slow failure in triaxially deformed Etna basalt using 3D acoustic-emission location and X-ray computed tomography. *Geophysical Research Letters*, 34, L03303. <https://doi.org/10.1029/2006GL028721>
- Bonaccorso, A. (1996). Dynamic inversion of ground deformation data for modelling volcanic sources (Etna 1991–93). *Geophysical research Letters*, 23(5), 451–454.
- Bonaccorso, A., Cianetti, S., Giunchi, C., Trasanti, E., Bonafede, M., & Boschi, E. (2005). Analytical and 3-D numerical modelling of Mt. Etna (Italy) volcano inflation. *Geophysical Journal International*, 163(2), 852–862. <https://doi.org/10.1111/j.1365-246X.2005.02777.x>
- Bonaccorso, A., Currenti, G., Del Negro, C., & Boschi, E. (2010). Dike deflection modelling for inferring magma pressure and withdrawal, with application to Etna 2001 case. *Earth and Planetary Science Letters*, 293(1–2), 121–129. <https://doi.org/10.1016/j.epsl.2010.02.030>
- Bonforte, A., Bonaccorso, A., Guglielmino, F., Palano, M., & Puglisi, G. (2008). Feeding system and magma storage beneath Mt. Etna as revealed by recent inflation/deflation cycles. *Journal of Geophysical Research*, 113, B05406. <https://doi.org/10.1029/2007JB005334>
- Branca, S., Coltelli, M., Groppelli, G., & Lentini, F. (2011). Geological map of Etna volcano, 1:50,000 scale. *Italian Journal of Geosciences*, 130(3), 265–291.
- Browning, J., Meredith, P., & Gudmundsson, A. (2016). Cooling-dominated cracking in thermally stressed volcanic rocks. *Geophysical Research Letters*, 43, 8417–8425. <https://doi.org/10.1002/2016GL070532>
- Browning, J., Meredith, P., Stuart, C. E., Healy, D., Harland, S., & Mitchell, T. (2017). Acoustic characterization of crack damage evolution in sandstone deformed under conventional and true triaxial loading. *Journal of Geophysical Research: Solid Earth*, 122, 4395–4412. <https://doi.org/10.1002/2016JB013646>
- Dautriat, J., Gland, N., Dimanov, A., & Raphanel, J. (2011). Hydromechanical behavior of heterogeneous carbonate rock under proportional triaxial loadings. *Journal of Geophysical Research*, 116, B01205. <https://doi.org/10.1029/2009JB000830>
- Day, S. J. (1996). Hydrothermal pore fluid pressure and the stability of porous, permeable volcanoes. *Geological Society, London, Special Publications*, 110(1), 77–93. <https://doi.org/10.1144/GSL.SP.1996.110.01.06>
- De Vries, B. V. W., & Borgia, A. (1996). The role of basement in volcano deformation. *Geological Society, London, Special Publications*, 110(1), 95–110. <https://doi.org/10.1144/GSL.SP.1996.110.01.07>

- Delaney, P. T., & Pollard, D. D. (1982). Solidification of basaltic magma during flow in a dike. *American Journal of Science*, 282(6), 856–885.
- Dieterich, J. H. (1988). Growth and persistence of Hawaiian volcanic rift zones. *Journal of Geophysical Research*, 93, 4258–4270. <https://doi.org/10.1029/JB093iB05p04258>
- Elsworth, D., & Day, S. J. (1999). Flank collapse triggered by intrusion: The Canarian and Cape Verde archipelagoes. *Journal of Volcanology and Geothermal Research*, 94(1–4), 323–340. [https://doi.org/10.1016/S0377-0273\(99\)00110-9](https://doi.org/10.1016/S0377-0273(99)00110-9)
- Elsworth, D., & Voight, B. (1992). Theory of dike intrusion in a saturated porous solid. *Journal of Geophysical Research*, 97(B6), 9105–9117.
- Evans, B., Fredrich, J. T., & Wong, T.-f. (1990). The brittle-ductile transition in rocks: Recent experimental and theoretical progress, 56, 1–20.
- Evans, B., & Kohlstedt, D. L. (1995). *Rheology of rocks*, 3, 148–165.
- Fazio, M., Benson, P. M., & Vinciguerra, S. (2017). On the generation mechanisms of fluid-driven seismic signals related to volcano-tectonics. *Geophysical Research Letters*, 44, 734–742. <https://doi.org/10.1002/2016GL070919>
- Fredrich, J. T., & Wong, T.-f. (1986). Micromechanics of thermally induced cracking in three crustal rocks. *Journal of Geophysical Research*, 91(B12), 12,743–12,764. <https://doi.org/10.1029/JB091iB12p12743>
- Gambino, S., Cannata, A., Cannavò, F., La Spina, A., Palano, M., Sciotto, M., et al. (2016). The unusual 28 December 2014 dike-fed paroxysm at Mount Etna: Timing and mechanism from a multidisciplinary perspective. *Journal of Geophysical Research: Solid Earth*, 121, 2037–2053. <https://doi.org/10.1002/2015JB012379>
- Griffiths, L., Lengliné, O., Heap, M. J., Baud, P., & Schmittbuhl, J. (2018). Thermal cracking in westerly granite monitored using direct wave velocity, coda wave interferometry and acoustic emissions. *Journal of Geophysical Research: Solid Earth*, 123, 2246–2261. <https://doi.org/10.1002/2017JB015191>
- Gudmundsson, A. (1995). Infrastructure and mechanics of volcanic systems in Iceland. *Journal of Volcanology and Geothermal Research*, 64(1–2), 1–22.
- Gudmundsson, A. (2002). Emplacement and arrest of sheets and dykes in central volcanoes. *Journal of Volcanology and Geothermal Research*, 116(3–4), 279–298.
- Guéguen, Y., & Palciauskas, V. (1994). *Introduction to the Physics of Rocks*. Princeton University Press.
- Harnett, C. E., Benson, P. M., Rowley, P., & Fazio, M. (2018). Fracture and damage localization in volcanic edifice rocks from El Hierro, Stromboli and Tenerife. *Nature Scientific Reports*, 8(1), 1942. <https://doi.org/10.1038/s41598-018-20442-w>
- Heap, M. J., Mollo, S., Vinciguerra, S., Lavallée, Y., Hess, K. U., Dingwell, D. B., et al. (2013). Thermal weakening of the carbonate basement under Mt. Etna volcano (Italy): Implications for volcano instability. *Journal of Volcanology and Geothermal Research*, 250, 42–60. <https://doi.org/10.1016/j.jvolgeores.2012.10.004>
- Kohlstedt, D. L., Evans, B., & Mackwell, S. J. (1995). Strength of the lithosphere: Constraints imposed by laboratory experiments. *Journal of Geophysical Research*, 100(B9), 17,587–17,602. <https://doi.org/10.1029/95JB01460>
- Lawn, B. R. (1993). *Fracture of Brittle Solids*, (2nd ed.). New York: Cambridge University Press. <https://doi.org/10.1017/CBO9780511623127>
- Lentini, F., & Carbone, S. (2014). Geologia della Sicilia-Geology of Sicily. *Memorie Descr. Carta Geologica d'Italia*, 95, 7–414.
- Lentini, F., Carbone, S., Guarnieri, P., Dilek, Y., & Pavlides, S. (2006). Collisional and postcollisional tectonics of the Apenninic-Maghrebian orogen (southern Italy). *Geological Society of America, Special Papers*, 409, 57.
- Mattia, M., Bruno, V., Caltabiano, T., Cannata, A., Cannavò, F., D'Alessandro, W., et al. (2015). A comprehensive interpretative model of slow slip events on Mt. Etna's eastern flank. *Geochemistry, Geophysics, Geosystems*, 16, 635–658. <https://doi.org/10.1002/2014GC005585>
- Mavko, G., Mukerji, T., & Dyorkin, J. (1998). *The Rock Physics Handbook. Tools for Seismic Analysis in Porous Media* (329 pp.). Cambridge: Cambridge University Press.
- McGuire, W. J. (1996). Volcano instability: A review of contemporary themes. *Geological Society, London, Special Publications*, 110(1), 1–23. <https://doi.org/10.1144/GSL.SP.1996.110.01.01>
- Mollo, S., Vinciguerra, S., Iezzi, G., Iarocci, A., Scarlato, P., Heap, M. J., & Dingwell, D. B. (2011). Volcanic edifice weakening via devolatilization reactions. *Geophysical Journal International*, 186(3), 1073–1077. <https://doi.org/10.1111/j.1365-246X.2011.05097.x>
- Nicolas, A., Fortin, J., Regnet, J. B., Dimanov, A., & Guéguen, Y. (2016). Brittle and semi-brittle behaviours of a carbonate rock: Influence of water and temperature. *Geophysical Journal International*, 206(1), 438–456. <https://doi.org/10.1093/gji/ggw154>
- Paterson, M., & Wong, T.-f. (2005). *Experimental rock deformation - the brittle field*, (2nd ed.). New York: Springer-Verlag.
- Reid, M. E., Sisson, T. W., & Brien, D. L. (2001). Volcano collapse promoted by hydrothermal alteration and edifice shape, Mount Rainier, Washington. *Geology*, 29(9), 779–782. [https://doi.org/10.1130/0091-7613\(2001\)029<0779:VCPBHA>2.0.CO;2](https://doi.org/10.1130/0091-7613(2001)029<0779:VCPBHA>2.0.CO;2)
- Rutter, E. H. (1972). The influence of interstitial water on the rheological behaviour of calcite rocks. *Tectonophysics*, 14(1), 13–33. [https://doi.org/10.1016/0040-1951\(72\)90003-0](https://doi.org/10.1016/0040-1951(72)90003-0)
- Rutter, E. H. (1974). The influence of temperature, strain rate and interstitial water in the experimental deformation of calcite rocks. *Tectonophysics*, 22(3–4), 311–334. [https://doi.org/10.1016/0040-1951\(74\)90089-4](https://doi.org/10.1016/0040-1951(74)90089-4)
- Sammonds, P. R. (1999). Understanding the fundamental physics governing the evolution and dynamics of the Earth's crust and ice sheets. *Philosophical Transactions of the Royal Society A: Mathematical, Physical and Engineering Sciences*, 357(1763), 3377–3401. <https://doi.org/10.1098/rsta.1999.0499>
- Siegesmund, S., Ullemeyer, K., Weiss, T., & Tschegg, E. K. (2000). Physical weathering of marbles caused by anisotropic thermal expansion. *International Journal of Earth Sciences*, 89(1), 170–182. <https://doi.org/10.1007/s005310050324>
- Sigmundsson, F., Hreinsdóttir, S., Hooper, A., Árnadóttir, T., Pedersen, R., Roberts, M. J., et al. (2010). Intrusion triggering of the 2010 Eyjafjallajökull explosive eruption. *Nature*, 468(7322), 426–430. <https://doi.org/10.1038/nature09558>
- Tuttle, O. F. (1949). The variable inversion temperature of quartz as a possible geologic thermometer. *American Mineralogist*, 34, 723–730.
- Vajdova, V., Baud, P., & Wong, T.-f. (2004). Compaction, dilatancy, and failure in porous carbonate rocks. *Journal of Geophysical Research*, 109, B05204. <https://doi.org/10.1029/2003JB002508>
- Vajdova, V., Zhu, W., Natalie Chen, T.-M., & Wong, T.-f. (2010). Micromechanics of brittle faulting and cataclastic flow in Tavel limestone. *Journal of Structural Geology*, 32(8), 1158–1169. <https://doi.org/10.1016/j.jsg.2010.07.007>
- Van Wyk De Vries, B., & Borgia, A. (1996). The role of basement in volcano deformation. *Geological Society, London, Special Publications*, 110, 95–110.
- Voight, B., & Elsworth, D. (1997). Failure of volcano slopes. *Geotechnique*, 47(1), 1–31. <https://doi.org/10.1680/geot.1997.47.1.1>
- Wiesmaier, S., Heap, M. J., Branca, S., Gilg, H. A., Kueppers, U., Hess, K. U., et al. (2015). Variability in composition and physical properties of the sedimentary basement of Mt Etna, Italy. *Journal of Volcanology and Geothermal Research*, 302, 102–116. <https://doi.org/10.1016/j.jvolgeores.2015.06.011>
- Wong, T.-f., & Baud, P. (2012). The brittle-ductile transition in porous rock: A review. *Journal of Structural Geology*, 44, 25–53. <https://doi.org/10.1016/j.jsg.2012.07.010>
- Yavuz, H., Demirdag, S., & Caran, S. (2010). Thermal effect on the physical properties of carbonate rocks. *International Journal of Rock Mechanics and Mining Sciences*, 47(1), 94–103. <https://doi.org/10.1016/j.ijrmms.2009.09.014>